Mitigating a TDP-43 proteinopathy using RNA-targeting CRISPR effector proteins

M. Alejandra Zeballos C.[1], Hayden J. Moore[1], Jackson E. Powell[1], Tyler J. Smith[1], Sijia Zhang[1], and Thomas Gaj[1,2,*]

[1] Department of Bioengineering, University of Illinois Urbana-Champaign, Urbana, IL 61801, USA

[2] Carl R. Woese Institute for Genomic Biology, University of Illinois Urbana-Champaign, Urbana, IL 61801, USA

[*] Corresponding author. Email: gaj@illinois.edu

ABSTRACT

The TDP-43 proteinopathies, which include amyotrophic lateral sclerosis and frontotemporal dementia, are a devastating group of neurodegenerative disorders that are characterized by the mislocalization and aggregation of TDP-43. Here we demonstrate that RNA-targeting CRISPR effector proteins, a programmable class of gene silencing agents that includes the Cas13 family of enzymes and Cas7-11, can be used to mitigate TDP-43 pathology when programmed to target ataxin-2, a modifier of TDP-43-associated toxicity. In addition to inhibiting the aggregation and transit of TDP-43 to stress granules, we find that the *in vivo* delivery of an ataxin-2-targeting Cas13 system to a mouse model of TDP-43 proteinopathy improved functional deficits, extended survival, and reduced the severity of neuropathological hallmarks. Further, we benchmark RNA-targeting CRISPR platforms against ataxin-2 and find that high-fidelity forms of Cas13 possess improved transcriptome-wide specificity compared to Cas7-11 and a first-generation effector. Our results demonstrate the potential of CRISPR technology for TDP-43 proteinopathies.

INTRODUCTION

The mislocalization and aggregation of TDP-43, a nuclear DNA/RNA binding protein involved in the regulation of transcription[1], is a cardinal feature of a group of neurodegenerative disorders known as the TDP-43 proteinopathies[1–6]. This includes nearly all cases of amyotrophic lateral sclerosis (ALS)[2,4], a disorder characterized by the deterioration of motor neurons in the brain and spinal cord[7], as well as the most common subtype of frontotemporal dementia (FTD)[2,4], a syndrome involving the degeneration of the frontal and/or temporal lobes of the brain. Though the exact pathological role of TDP-43 in ALS-FTD and other TDP-43 proteinopathies remains incompletely understood, it's believed that its depletion from the nucleus and/or its abnormal deposition into cytoplasmic inclusions may give rise to gain and/or loss of functions that drive its toxicity[1,8–10], a hypothesis supported by the discovery that its mutation is also associated with disease[11–14].

However, despite its central role in neurodegeneration, numerous lines of evidence suggest that TDP-43 may not be an appropriate target for therapeutic silencing, as it plays a key role in numerous cellular processes[15] and its depletion from cells can induce various side effects[16–19]. Instead, attempts have been undertaken to identify modifier(s) whose targeting can attenuate the apparent toxic effects induced by aberrant TDP-43 without affecting its levels[20–24]. One such modifier is ataxin-2[20,25,26], a polyglutamine-containing RNA binding protein thought to be involved in regulating mRNA translation[27] that, when mutated to carry an intermediate-length polyglutamine expansion, also emerges as a risk factor for ALS[20,28–32]. Importantly, the potential for ataxin-2 as a therapeutic target is supported by several lines of evidence, including that its downregulation in yeast and flies decreases TDP-43-associated toxicity[20] and that its genetic ablation in a rodent model of TDP-43 proteinopathy can mitigate pathological features without

affecting TDP-43 expression[26]. Strategies for modulating the expression of ataxin-2 may thus hold potential for ALS-FTD and other TDP-43 proteinopathies.

In addition to traditional gene silencing modalities, CRISPR technologies have emerged as effective platforms capable of perturbing the expression of a target gene[33–35], including potentially ataxin-2. Among the CRISPR-based platforms that can be used for this goal are RNA-targeting CRISPR effector proteins[36–42], which rely on an engineered CRISPR RNA (crRNA) molecule to recognize a target RNA sequence that facilitates its degradation by the CRISPR protein. This continuously expanding group of effector proteins includes the Cas13 family of enzymes[36,38–41] which, after binding to a target RNA sequence, have the capacity to indiscriminately *trans*-cleave non-target RNAs, as well as Cas7-11[43], a protein that cleaves its target RNA in *cis* and as such is thought to pose minimal risk for collaterally *trans*-cleaving RNA. Given their programmability and their capacity to knock down the expression of a target gene in mammalian cells[36,41], we hypothesized that RNA-targeting CRISPR effectors could be harnessed to target ataxin-2 for the goal of attenuating a TDP-43 proteinopathy.

Here we show that, when programmed to target ataxin-2, RNA-targeting CRISPR effectors are capable of mitigating TDP-43 pathology. In addition to inhibiting the aggregation and transit of the TDP-43 protein to stress granules – highly dynamic intracellular accumulations of protein and RNA that are thought to play a role in ALS-FTD[44–46] – we demonstrate that this class of effector proteins can be used to slow disease progression *in vivo*. Specifically, we find that delivering an ataxin-2-targeting Cas13 protein to a mouse model of TDP-43 proteinopathy decreased ataxin-2 mRNA in the brain, which improved functional deficits, increased survival, and reduced the severity of several neuropathological hallmarks. Further, we benchmark recently emerged RNA-targeting CRISPR effector platforms against ataxin-2 and find that high-fidelity

forms of the Cas13 protein possess improved targeting specificity compared to Cas7-11 and a first-generation Cas13 protein.

Our results demonstrate the potential of CRISPR technologies for TDP-43 proteinopathies and reinforce the role of ataxin-2 as a modifier of TDP-43 toxicity.

RESULTS

Targeting ataxin-2 with RfxCas13d

Because of its ability to influence TDP-43-associated toxicity[20,25,26], ataxin-2 has emerged as a potentially broadly applicable target for ALS-FTD, as TDP-43 pathology is observed in ~97% of ALS cases[1,4,5] and ~45% FTD occurrences[1,2,4]. Given this, we sought to determine if RNA-targeting CRISPR effector proteins could be used to lower the expression of ataxin-2 to mitigate TDP-43-mediated toxicity. As overexpression of the human TDP-43 protein in mice can result in a phenotype reminiscent of ALS that can be attenuated by the knockout of its ataxin-2 gene[26], we initially targeted the mouse ataxin-2 (mATXN2) transcript (**Fig. 1a**) to ensure that this strategy could be assessed in a validated rodent model.

To target the mATXN2 mRNA, we used the Cas13d nuclease from *Ruminococcus flavefaciens* XPD3002 (RfxCas13d)[41], a programmable RNA-targeting effector protein that we[47] and others[48,49] have demonstrated can silence target gene expression in the nervous system. To facilitate the identification of crRNAs for mATXN2, we created a reporter plasmid carrying the mATXN2 protein-coding sequence fused to an enhanced green fluorescence protein (EGFP) via a self-cleaving T2A peptide, linking mATXN2 expression to EGFP fluorescence. Following the design of ten crRNAs to target mATXN2 (**Fig. 1b**), we transfected human embryonic kidney (HEK) 293T cells with expression vectors encoding RfxCas13d and a mATXN2-targeting crRNA

alongside the mATXN2-T2A-EGFP-encoding plasmid. Based on flow cytometry, we found that all ten of the crRNAs decreased EGFP fluorescence by >50% compared to a non-targeted crRNA at 48 hr post-transfection ($P < 0.0001$; **Fig. 1c**), with the most active crRNA, the exon 15-targeting crRNA-10, found to decrease EGFP fluorescence by ~87% ($P < 0.0001$, **Fig. 1c**). Conveniently, we also found that crRNA-6, a crRNA whose target in mATXN2 is perfectly homologous to the equivalent site in human ATXN2 (hATXN2) (**Fig. 1a**), decreased EGFP fluorescence by ~87% ($P < 0.0001$, **Fig. 1c**), indicating its potential as a platform for targeting the human ortholog.

We next evaluated if RfxCas13d could knock down the endogenous mATXN2 transcript and if its targeting induced collateral effects in cells, as RfxCas13d-mediated *trans*-cleavage can lead to the degradation of non-specific RNA[50–54]. To answer this first question, we transfected Neuro2A mouse neuroblastoma cells with RfxCas13d and crRNA-10, the most efficient mATXN2-targeting crRNA identified from our initial screen. According to qPCR, which we used to measure mATXN2 mRNA, we found that RfxCas13d reduced mATXN2 mRNA by ~50% compared to cells transfected with a non-targeted (NTG) crRNA ($P < 0.05$, **Fig. 1d**).

To measure potential collateral effects, we transfected Neuro2A cells with RfxCas13d and crRNA-10 alongside an mCherry-encoding surrogate reporter, whose fluorescence was used as proxy for collateral activity (e.g., by this method[50–54] collateral *trans*-cleavage by RfxCas13d is expected to decrease mCherry fluorescence). Relative to cells transfected with mCherry alongside an inert carrier plasmid, we measured no significant decrease in the percentage of $mCherry^+$ cells or mCherry fluorescence intensity in cells transfected with RfxCas13d and crRNA-10 ($P > 0.05$ for both, **Supplementary Fig. 1a, b**).

Thus, our results demonstrate that RfxCas13d can be programmed to target mATXN2 mRNA. Further, we find that RfxCas13d can target the endogenous mATXN2 transcript without

decreasing the fluorescence of mCherry, a surrogate reporter that we used as a proxy for collateral activity.

RfxCas13d targeting can attenuate the formation of TDP-43 aggregates

In addition to its role in coordinating protein translation, the ataxin-2 protein can regulate the formation of stress granules (SGs)[26,44,55], highly dynamic cytoplasmic structures that form in response to cellular stress and are implicated in various neurodegenerative disorders[44–46]. As knocking down ataxin-2 can reduce the susceptibility of TDP-43 to localize to SGs[26], we next determined if targeting ataxin-2 by RfxCas13d could also inhibit the recruitment of TDP-43 to these structures and decrease its propensity to form aggregates[26,44,55–58].

Because TDP-43 does not strongly localize with SGs in Neuro2A cells[59], we instead evaluated the ability of RfxCas13d to inhibit TDP-43 aggregation in HEK293T cells which, when treated with the oxidative stressor sorbitol, can form TDP-43^{+} SGs[44]. We transfected HEK293T cells with RfxCas13d and crRNA-6, the crRNA whose target site in the mATXN2 mRNA matches the equivalent site in the human ortholog and whose action we determined could decrease hATXN2 mRNA in HEK293T cells by ~40% ($P < 0.005$; **Supplementary Fig. 2**). We then induced the formation of SGs by exposing the transfected cells to 0.4 M of sorbitol for 1 hr prior to permeabilization **(Fig. 2a**).

Using an immunofluorescent analysis, we found that cells treated with RfxCas13d and the hATXN2-targeting crRNA-6 had ~42% less TDP-43^{+} inclusions per cell compared to control cells, which we transfected with RfxCas13d and a non-targeted crRNA ($P < 0.005$, **Fig. 2b, c**). Further, we measured that RfxCas13d with crRNA-6 decreased the overall percentage of cells with detectable TDP-43 inclusions by ~28% ($P < 0.05$, **Fig. 2b, d**) and that, for those cells with

detectable TDP-43 inclusions, RfxCas13d reduced the average size of those inclusions by ~47% ($P < 0.01$, **Fig. 2b, e**). Critically, we also observed that cells treated with RfxCas13d had a ~43% decrease in the number of cells with foci positive for both TDP-43 and the SG marker G3BPI[60] (Ras-GAP SH3-domain-binding protein 1; $P < 0.05$; **Fig. 2b, f**), providing evidence that RfxCas13d-mediated targeting of hATXN2 decreased the transit of TDP-43 to SGs.

We next evaluated if targeting hATXN2 by RfxCas13d could influence the aggregation of TDP-43 mutants that have been linked to ALS[11]. We thus transfected HEK293T cells with RfxCas13d and crRNA-6 alongside one of three reporter plasmids each expressing a distinct TDP-43 variant (TDP-43^{A315T}, TDP-43^{G298S} or TDP-43^{M337V}) with a propensity to misfold and aggregate[61,62]. To enable the microscopic visualization of TDP-43 aggregation, each variant was fused to the yellow fluorescent protein (YFP). Notably, these three TDP-43 mutations are among the five most common ALS-linked mutations in TDP-43 and are located in the Gly-rich C-terminal domain of the protein, a region thought to mediate protein-protein interactions[12,63,64] and contribute to the association of TDP-43 with SGs[44].

According to our immunofluorescent analysis, we found that RfxCas13d broadly decreased the size of the YFP-TDP-43 inclusions. In the case of TDP-43^{A315T}, we measured that RfxCas13d decreased the average size of inclusions by ~41% ($P < 0.05$; **Supplementary Fig. 2a, d**) and reduced the average number of those inclusions in HA^{+} cells by ~45% ($P < 0.05$; **Supplementary Fig. 2a, e)** while, for TDP-43^{G298S} and TDP-43^{M337V}, RfxCas13d decreased the size of detectable inclusions by ~15% ($P < 0.05$ for both; **Supplementary Fig. 2b, c, f, g**).

To rule out the possibility that the reduction in YFP-TDP-43^{+} inclusions was attributable to collateral *trans*-cleavage of the YFP-TDP-43 transcript, we co-transfected HEK293T cells with RfxCas13d and crRNA-6 in the presence of the YFP-TDP-43 reporter and an mCherry-encoding

surrogate reporter, whose fluorescence was used as a second proxy for collateral targeting. Flow cytometry showed no changes in fluorescence intensity for either mCherry or YFP in cells transfected with RfxCas13d with crRNA-6 versus the controls ($P > 0.05$; **Supplementary Fig. 4**), indicating that the reduction in the TDP-43 inclusions was likely not attributable to collateral effects.

Altogether, these results demonstrate that RfxCas13d-mediated targeting of hATXN2 can influence the formation of the TDP-43 aggregates implicated in ALS.

Targeting ATXN2 *in vivo* by RfxCas13d can reduce a TDP-43 pathology

We next sought to determine the therapeutic benefit of targeting ATXN2 by RfxCas13d in a transgenic mouse model of a TDP-43 proteinopathy, specifically homozygous TAR4/4 mice, which overexpress the wild-type human TDP-43 (hTDP-43) protein under the control of a murine Thy-1 (mThy-1) promoter[65]. TAR4/4 mice develop a quadriplegia phenotype reminiscent of ALS and have an average lifespan of ~24 days[65], which can necessitate early intervention.

To deliver RfxCas13d, we used adeno-associated virus serotype 9 (AAV9) which, when administrated to neonatal mice via intravenous (IV)[66] and intracerebroventricular (ICV)[67] injections, can access neurons in the brain and spinal cord. However, prior to delivering RfxCas13d to TAR4/4 mice, we administered it to wild-type animals to evaluate its distribution and targeting in a healthy background. Postnatal day 1-2 (P1-2) B6SJLF1/J mice were thus infused with an AAV9 vector encoding RfxCas13d, driven by a CBh promoter, with a mATXN2-targeting crRNA (AAV9-CBh-RfxCas13d-mATXN2) or a non-targeted crRNA (AAV9-CBh-RfxCas13d-NTG) via both the facial vein (7×10^{11} vector genomes [vg] per pup) and the lateral ventricles (8.4×10^{10}

vg per pup) (**Fig. 3a**), as combining IV and ICV injections has been demonstrated as an effective strategy for enhancing AAV9 delivery to the nervous system of neonatal mice[68–70].

Using its hemagglutinin epitope (HA) tag for detection, we observed at four weeks post-injection that RfxCas13d was present throughout the brain, including in the motor, somatosensory and visual cortices (MC, SC and VC respectively), the brainstem (BS), the striatum (STR), the hippocampus (HPC), the cerebellum (CBM), and the spinal cord (SC; **Fig. 3b-e and Supplementary Fig. 5a-d**), with its expression largely confined to $NeuN^+$ cells (**Fig. 3b, d, f and Supplementary Fig. 5a-d, f**).

To evaluate RfxCas13d-mediated targeting, we used qPCR to measure mATXN2 mRNA in several of the most strongly transduced areas, including the MC, the STR, the BS, the HPC and the VC. Compared to animals injected with the non-targeted vector, mice injected with AAV9-CBh-RfxCas13d-mATXN2 had a ~54%, a ~30%, a ~40%, a ~33% and a ~50% decrease in relative mATXN2 mRNA in the MC, the BS, the STR, the HPC, and the VC respectively ($P < 0.05$ for MC, BS, HPC; $P < 0.01$ for STR; $P < 0.001$ for VC; **Fig. 3g and Supplementary Fig. 5e**), indicating that RfxCas13d could suppress mATXN2 expression *in vivo*.

We next determined if RfxCas13d could influence TDP-43 pathology by injecting P1-2 TAR4/4 mice with AAV9-CBh-RfxCas13d-mATXN2 or AAV9-CBh-RfxCas13d-NTG using the same dual administration strategy as described for B6SJLF1/J mice. In addition to abnormal gait and severe tremors, which typically begin manifesting at P14[65], TAR4/4 mice display a rapid and progressive decline in motor function and develop increasingly severe kyphosis[65], defined as a hunched posture resulting from a curved spine. We thus monitored these phenotypes, as well as weight and lifespan, which are also adversely affected in TAR4/4 mice[65] to gauge the effect of RfxCas13d.

Compared to control animals, we found that TAR4/4 mice infused with AAV9-CBh-RfxCas13d-mATXN2 had improved gait ($P < 0.05$; **Fig. 4a**), decreased kyphosis ($P < 0.05$; **Fig. 4b**), reduced tremors ($P < 0.05$; **Fig. 4c)** and increased weight ($P < 0.05$; **Fig. 4d**). We also found that these same mice possessed improved neuromuscular function and motor coordination, as animals treated with RfxCas13d were able to attain higher maximum speeds on an accelerating rotarod ($P < 0.05$; **Fig. 4e**) and displayed improved forelimb grip strength ($P < 0.05$; **Fig. 4f**) relative to animals injected with the control vector. Additionally, and most strikingly, we found that TAR4/4 mice treated with the AAV9-CBh-RfxCas13d-mATXN2 had a ~35 day increase in mean survival compared to the control mice (mATXN2: 61.56 ± 13.89 days; NTG: 26 ± 2.6 days; $P < 0.05$; **Fig. 4g**), with several treated TAR4/4 mice found to survive for over 80 days.

Consistent with our findings in B6SJLF1/J mice, we observed by an immunofluorescent analysis that RfxCas13d was expressed throughout the brain in end-stage TAR4/4 mice (**Fig. 5a**). Further, a qPCR analysis of these end-stage tissues revealed that mice injected with AAV9-CBh-RfxCas13d-mATXN2 had ~40% and ~30% less mATXN2 mRNA in the MC and BS, respectively, compared to mice injected with the non-targeted vector ($P < 0.01$ for MC and $P < 0.05$ for BS; **Fig. 5b**), indicating that RfxCas13d suppressed mATXN2 expression in TAR4/4 mice. Critically, we also measured by qPCR no significant difference in relative hTDP-43 mRNA between treated and control animals in the MC and BS ($P > 0.05$ both; **Fig. 5c**), suggesting that RfxCas13d affected disease progression without significantly affecting the expression of hTDP-43.

Last, we evaluated if RfxCas13d affected neuropathological hallmarks in TAR4/4 mice. In addition to neuronal loss, TAR4/4 mice accumulate phosphorylated and ubiquitinated forms of TDP-43 and develop prominent microgliosis and astrogliosis by P24, their average end-point[65]. Using immunofluorescent analysis, we found that mice injected with AAV9-CBh-RfxCas13d-

mATXN2 had ~23% more NeuN$^+$ cells in the MC at end-stage compared to mice infused with the non-targeted vector ($P < 0.05$; **Fig. 5d, e**). Additionally, when probed with a phospho-TDP-43-specific antibody that binds to the pathological species[71], we found that TAR4/4 mice injected with AAV9-CBh-RfxCas13d-mATXN2 had a ~62% decrease in NeuN$^+$ cells with detectable soluble pTDP-43 compared to untreated mice ($P < 0.01$; **Fig. 5d, f and Supplementary Fig. 6**) and that, within the NeuN$^+$ cell populations, treated animals had ~61% and a ~27% fewer pTDP-43$^+$ and ubiquitin$^+$ inclusions, respectively, compared to control animals ($P < 0.05$ for both; **Fig. 5g and Supplementary Fig. 6**). Finally, we used immunofluorescent analysis to examine microgliosis and astrogliosis, observing that mice injected with AAV9-CBh-RfxCas13d-mATXN2 had a ~36% and a ~34% reduction in the number of Iba1$^+$ and GFAP$^+$ cells in layer V of the MC, respectively ($P < 0.05$ for both; **Supplementary Fig. 7**), indicating that targeting mATXN2 reduced neuroinflammation.

Our results demonstrate that RfxCas13d can be delivered to the nervous system by AAV9, that RfxCas13d can lower mATXN2 mRNA *in vivo*, and that its action in TAR4/4 mice can improve impairments, slow disease progression, and affect hallmarks of TDP-43 pathology.

High-fidelity Cas13 and Cas7-11 can target ataxin-2

Upon binding to its target RNA, RfxCas13d – like other Cas13 effectors – can collaterally cleave non-target RNAs[50,52–54]. Because of this, high-fidelity (Hi-Fi) forms of the protein have been developed that possess a reduced capacity to *trans*-cleave non-target RNAs, while still retaining the ability to cleave target RNA[72]. Additionally, and in contrast to the Cas13 family of enzymes, DiCas7-11, a sub-type III-E effector protein from *Desulfonema ishimotonii*, can mediate crRNA-dependent RNA knockdown by a mechanism that appears to occur in *cis* and thus is

thought to pose minimal risk for collateral activity[43]. Given their features, we determined if Hi-Fi versions of the RfxCas13d protein, as well as the *cis*-cleaving protein DiCas7-11, could be used to target ataxin-2 and if their implementation would lead to fewer off-target effects than RfxCas13d.

The extent with which Cas13 enzymes can collaterally cleave RNAs can correlate with the expression threshold of the target transcript, with targeting of an overexpressed mRNA thought to result in more robust collateral effects[50–53]. Knowing this, we evaluated the targeting capabilities of the Hi-Fi RfxCas13d variants, RfxCas13d-N1V7, -N2V7 and -N2V8, as well as DiCas7-11, in HEK293T cells transiently transfected with the mATXN2-T2A-EGFP-encoding reporter plasmid alongside an mCherry-encoding reporter, whose fluorescence was used as a proxy for collateral targeting. Consistent with prior studies demonstrating that targeting highly expressed reporter transcripts in mammalian cells can lead to robust collateral effects[50–54], we found that, when programmed to target mATXN2-T2A-EGFP, the native RfxCas13d protein reduced mCherry fluorescence by ~40-60% ($P < 0.001$; **Fig. 6a and Supplementary Fig. 8**), indicating collateral cleavage in the context of the transient overexpression assay. However, when paired with the same crRNAs, we measured that the Hi-Fi forms of RfxCas13d reduced these collateral effects (**Fig. 6b-d**), with RfxCas13d-N2V7 found as the variant most effective at decreasing mATXN2-T2A-EGFP without affecting mCherry fluorescence ($P > 0.001$; **Fig. 6c**). Similarly, when programmed to target the same sequences as the RfxCas13d variants, we found that the *cis*-cleaving enzyme DiCas7-11 could also decrease EGFP without diminishing mCherry fluorescence (**Fig. 6e**); however, for the pool of crRNAs examined, DiCas7-11 was generally less efficient than the Hi-Fi forms of RfxCas13d (**Fig. 6e**).

We next determined the ability of RfxCas13d-N2V7 (hereafter referred to as HiFi-RfxCas13d) and DiCas7-11 to target the endogenous mATXN2 transcript. According to qPCR,

we found that both HiFi-RfxCas13d and DiCas7-11 lowered mATXN2 mRNA by ~50-55% in Neuro2A cells when paired with crRNA-10 ($P < 0.05$ for HiFi-RfxCas13d; $P < 0.01$ for DiCas7-11; **Fig. 6f**), which was on par with our measurements for the native RfxCas13d protein (**Fig. 1d**).

To compare their transcriptome-wide specificities, we conducted an RNA-seq analysis on Neuro2A cells transfected with the RfxCas13d, HiFi-RfxCas13d and DiCas7-11 alongside their respective mATXN2-targeting crRNA. All three variants exhibited favorable specificity when programmed to target the endogenous mATXN2 transcript; however, HiFi-RfxCas13d affected fewer genes (273) compared to DiCas7-11 (659 genes) and RfxCas13d (727 genes; >1-fold change [FC], FDR-adjusted P-value < 0.05 for all; (**Fig. 6g, h**), indicating that, in this context, HiFi-RfxCas13d possessed the highest transcriptome-wide specificity.

Finally, because of its favorable targeting characteristics, we evaluated if HiFi-RfxCas13d could inhibit TDP-43 aggregation. We therefore transfected HEK293T cells with HiFi-RfxCas13d and crRNA-6 (i.e., the hATXN2-targeting crRNA) before exposing the cells to sorbitol to induce the formation of SGs. Similar to the native RfxCas13d protein, we measured by immunofluorescent analysis that HiFi-RfxCas13d decreased the size of TDP-43^{+} inclusions in transfected cells by ~28% compared to control cells ($P < 0.01$; **Fig. 6i)**.

To evaluate if HiFi-RfxCas13d could also prevent the formation of inclusions consisting of ALS-linked TDP-43 mutants, we transfected HEK293T cells with HiFi-RfxCas13d and crRNA-6 alongside a reporter expressing TDP-43^{A315T} linked to YFP, which enabled us to monitor the formation of pathological aggregates. Consistent with our observations for the native RfxCas13d protein, we found that HiFi-RfxCas13d reduced the average size of the TDP-43^{A315T+} inclusion by ~20% ($P < 0.05$; **Fig. 6j),** indicating that high-fidelity forms of Cas13 can influence a TDP-43 pathology in cell culture models.

In sum, we find that RNA-targeting CRISPR effector proteins can be programmed to target ataxin-2 and that lowering ataxin-2 mRNA with these platforms can mitigate aspects of TDP-43 pathology.

DISCUSSION

Because of their intrinsic RNase activity[36–42], their high programmability, and their ability to be used in mammalian cells to knock down the expression of a target gene[36,41,47–49,73], RNA-targeting CRISPR effector proteins are a potentially powerful class of agents for gene silencing. Here we demonstrate that two such RNA-targeting effector proteins – RfxCas13d[41,72] and DiCas7-11[43] – can be programmed to target ataxin-2, a polyglutamine-containing RNA binding protein whose downregulation can attenuate TDP-43-associated toxicity[20]. In particular, we find that RfxCas13d and a high-fidelity version of it can inhibit the formation of TDP-43^{+} aggregates in cell culture models of the pathology. Additionally, we show that the *in vivo* delivery of RfxCas13d to a mouse model of TDP-43 proteinopathy could provide broad therapeutic benefit, as RfxCas13d improved gait, kyphosis, tremors, weight loss, grip strength and rotarod performance, extended lifespan and decreased the severity of several neuropathological hallmarks, including neuronal survival, the accumulation of phosphorylated and ubiquitinated TDP-43, and microgliosis and astrogliosis. Our findings thus illustrate the potential of CRISPR technology for TDP-43 proteinopathies, which include ALS and FTD.

Though they affect different regions of the central nervous system, ALS and FTD are two conditions that are thought to exist on a continuous disease spectrum[1,6]. ALS, in particular, is a rapidly progressive disorder that affects motor neurons in the spinal cord and brain, resulting in the loss of muscle control, paralysis and ultimately death. At present, there is no cure for ALS and

current therapies provide limited benefit. While strategies for silencing dominantly inherited mutant genes causative for ALS, such as superoxide dismutase 1[47,74–76] or C9ORF72[77–79], hold promise for those familial forms of the disease, ~90% of ALS cases are sporadic, with few clear risk factors for targeting. This notwithstanding, ~97% of ALS cases are characterized by inclusions consisting of ubiquitinated and hyper-phosphorylated TDP-43[1–4], indicating it may play a central role in the pathophysiology of the disease, a finding that has helped to elevate its status as a therapeutic target. However, TDP-43 plays a key role in many cellular processes[15] and thus may not be an ideal target for silencing. Instead, attention has turned to the identification of modifier(s) whose targeting can attenuate the apparent toxic effects induced by aberrant TDP-43 but without affecting its underlying levels[20–24]. Ataxin-2 has emerged as one such candidate. While the exact mechanism by which ataxin-2 modifies TDP-43-associated toxicity has not been fully unraveled, strategies for targeting ataxin-2 nonetheless appear to hold potential for TDP-43 proteinopathies[26]. Notably, an antisense oligonucleotide (ASO) directed against ataxin-2 was found to lower the toxicity of TDP-43 in a transgenic mouse model of the pathology[26], with a related approach now under evaluation in a clinical trial (ClinicalTrials.gov Identifier: NCT04494256). However, despite their successes, ASOs possess drawbacks. Among them is their transient life cycle, which can result in periods of diminished efficacy that necessitates redosing, a caveat that can impose a physical burden on patients. For this reason, we explored the utility of RNA-targeting CRISPR proteins to target ataxin-2, as these platforms are genetically encodable and can be expressed from a viral vector to continuously engage with a target mRNA. Additionally, unlike their DNA editing counterparts, RNA-targeting CRISPR platforms offer, in theory, a reversible effect, which in the future could help to minimize risk.

Cas13 proteins, however, possess a limitation that can impact their potential therapeutic implementation: after engaging with a target transcript, they undergo a confirmational change that unlocks an ability to indiscriminately *trans*-cleave non-target RNAs[50,52–54]. This effect, known as collateral cleavage, has been observed against various endogenous targets[50,52–54] and its severity is believed to correlate with the expression threshold of the target transcript[50,52,53]. Given its importance, we measured the collateral activity of the native RfxCas13d protein in several contexts. Notably, when targeting endogenous ataxin-2 mRNA in Neuro2A or HEK293T cells, we observed no significant reduction in the fluorescence of the reporter protein(s) that we used as proxies for collateral cleavage; however, when tasked to target a strongly overexpressed mRNA target, we measured collateral cleavage, mirroring reports from the literature[50,52,53]. Such findings, in fact, have been the impetus for the development of Hi-Fi forms of RfxCas13d[72] and alternate RNA-targeting CRISPR effectors, such as Cas7-11[43]. Given their potential, we compared the targeting capabilities of several Hi-Fi variants, finding that, while Hi-Fi RfxCas13d could reduce collateral targeting in the context of the transient, overexpression-based reporter assay, their efficiency and *trans*-cleavage capabilities fluctuated based on the Hi-Fi variant used and the crRNA sequence employed, indicating there may exist a complex interplay between the target sequence recognized by the crRNA and the HiFi variant itself, a relationship that requires further study.

Interestingly, we observed no apparent side-effects from delivering the native RfxCas13d protein to TAR4/4 mice, instead finding that it broadly improved numerous therapeutic outcomes. Given the role that transcript threshold is thought to play on the strength of collateral activity, we hypothesize that the expression level of the endogenous mATXN2 transcript in the targeted cells may have been too low to trigger adverse effects, a hypothesis supported by our RNA-seq analysis,

which revealed that RfxCas13d affected the expression of 727 genes (>1-FC, FDR-adjusted P-value < 0.05), a number that was similar to that observed with DiCas7-11 (659), an enzyme that reportedly lacks the ability to *trans*-cleave non-target RNAs. Given the limited number of crRNAs used in this study, a more detailed investigation is needed in order to effectively compare RfxCas13d and its Hi-Fi equivalents with DiCas7-11.

This study is a proof-of-concept demonstrating the potential for RNA-targeting CRISPR technology to affect TDP-43 proteinopathy. Additional work is needed to identify optimal RNA-targeting CRISPR effector platforms for targeting ataxin-2, to determine their efficacy and safety in other ALS and FTD models, to evaluate the long-term consequences for silencing ataxin-2, and to establish if targeting ataxin-2 at the later stages of a disease can affect or reverse progression. In addition to the gene silencing modalities discussed here, traditional CRISPR nucleases and next-generation DNA editing technologies[80] could also conceivably be used to target ataxin-2, though RNA-targeting platforms offer the theoretical advantage of reversibility.

In conclusion, we demonstrate that RNA-targeting CRISPR effector proteins can be programmed to target ataxin-2, a potent modifier of TDP-43-associated toxicity, and that the *in vivo* delivery of an ataxin-2-targeting Cas13 system to a mouse model of TDP-43 proteinopathy could provide broad therapeutic benefit. Our results demonstrate the potential of CRISPR technology for TDP-43 proteinopathies.

METHODS

Plasmid construction

RfxCas13d and its crRNA were expressed from the previously described[47] plasmid pAAV-CAG-RfxCas13d-U6-crRNA.

To clone the reporter plasmid mATXN2-T2A-EGFP, PCR was used to amplify the T2A-EGFP sequence from pXR001 (Addgene #109049; a gift from Patrick Hsu[41]) using the T2A-GFP Gibson forward and reverse primers (**Supplementary Table 1)**. The ensuing amplicon was ligated into the EcoRV and PmeI restriction sites of pCMV-mATXN2-Myc-PolyA (MR218010, OriGene) by Gibson assembly using the Gibson Assembly Master Mix (New England Biolabs, NEB).

The plasmid encoding hTDP-43 fused to YFP (pcDNA3.2-hTDP-43-YFP) was a gift from Aaron Gitler (Addgene #84911). To construct the hTDP-43 mutant-carrying plasmids pcDNA3.2-hTDP-43^{A315T}-YFP, pcDNA3.2-hTDP-43^{M337V}-YFP and pcDNA3.2-hTDP-43^{G298S}-YFP, site-directed mutagenesis was conducted using the Q5 Site-Directed Mutagenesis Kit (NEB). Briefly, primers with single nucleotide substitutions encoding the A315T (GCG to ACG), G298S (GGT to AGT) and M337V (ATG to GTG) mutations were incubated with pcDNA3.2-TDP-43-YFP and Q5 Hot Start High-Fidelity DNA Polymerase, according to the manufacturer's instructions. The ensuing reaction product was incubated with the KLD enzyme mix for 5 min at room temperature (RT) and transformed to NEB 5-alpha *Escherichia coli.*

The plasmid used for AAV vector manufacturing, pAAV-CBh-RfxCas13d-U6-crRNA, was created by VectorBuilder by replacing the CAG promoter from pAAV-CAG-RfxCas13d-U6-crRNA[47] with a hybrid form of the chicken β-actin promoter (CBh) promoter[81,82].

To construct the plasmids encoding the HiFi-RfxCas13d (pAAV-CAG-RfxCas13d-N1V7-U6-crRNA, pAAV-CAG-RfxCas13d-N2V7-U6-crRNA, and pAAV-CAG-RfxCas13d-N2V8-

U6-crRNA), PCR was used to introduce HiFi mutations into the RfxCas13d gene sequence. Each variant was amplified as two fragments from pAAV-CAG-RfxCas13d-U6-crRNA using the primers: (1) Fusion_NcoI_Forward_v2 with Fusion_N1V7_R, Fusion_N2V7_R, or Fusion_N2V8_R; (2) Fusion_N1V7_F, Fusion_N2V7_F or Fusion_N2V8_F with Fusion_SacI_Reverse (**Supplementary Table 1)**. The fragments were then fused together by overlap PCR. Once assembled, each variant was ligated into the NcoI and SacI restriction sites of pAAV-CAG-RfxCas13d-U6-crRNA.

To clone the pAAV-CAG-DiCas7-11-U6-crRNA plasmid, PCR was used to amplify the U6-crRNA scaffold and the DiCas7-11 sequence from pDF0114 (Addgene #172508) and pDF0159 (Addgene #172507), respectively. Both plasmids were gifts from Omar Abudayyeh and Jonathan Gootenberg. The primers used to amplify the gene sequences were: NheI-U6_F and KpnI-polyT7-11_R for the U6-crRNA scaffold and F_DiCas7-11 and R_DiCas7-11 for the DiCas7-11 sequence. PCR was then used to separately amplify the sequence encoding the HA epitope from pAAV-CAG-RfxCas13d-U6-crRNA using the primers F_BsiWI_3HA and R_3HA. The amplicon encoding the U6-crRNA scaffold was ligated into the NheI and KpnI restriction sites of pAAV-CAG-RfxCas13d-U6-crRNA. The amplicons encoding DiCas7-11 and the HA epitope were fused by overlap PCR and ligated into the HindIII and AgeI restriction sites of pAAV-CAG-RfxCas13d-U6-crRNA, replacing RfxCas13d and its U6-crRNA sequence.

crRNA targeting sequences were cloned into their designated plasmids, as described[47]. Briefly. oligonucleotides encoding the crRNA sequences were custom synthesized (Integrated DNA Technologies) and incubated with T4 polynucleotide kinase (NEB) for 30 min at 37°C, annealed at 95°C for 5 min, and then cooled to 4°C at a rate of −0.1°C/s. Annealed oligonucleotides were then ligated into the BbsI restriction sites of pAAV-CAG-RfxCas13d-U6-crRNA, pAAV-

CAG-RfxCas13-U6-crRNA and pAAV-CAG-HiFi-RfxCas13d-U6-crRNA or the BsaI restriction sites of pAAV-CAG-DiCas7-11-U6-crRNA.

Sanger sequencing (ACGT) was used to confirm the identity of all plasmids. All primer sequences are provided in **Supplementary Table 1**.

Cell culture

HEK293T cells (American Type Culture Collection) and Neuro2A cells (a gift from Pablo Perez-Pinera) were maintained in Dulbecco's modified Eagle's medium (DMEM; Corning) supplemented with 10% (v/v) fetal bovine serum (FBS; Thermo Fisher Scientific) and 1% (v/v) antibiotic-antimycotic (Thermo Fisher Scientific) in a humidified 5% CO_2 incubator at 37°C. For all transfections, cells were seeded onto 24-well plates at an average density of 2×10^5 cells per well.

Cells were transfected with 450 ng of pAAV-CAG-RfxCas13d-U6-crRNA, pAAV-HiFi-RfxCas13d-U6-crRNA, or pAAV-DiCas7-11-U6-crRNA with 50 ng of mATXN2-T2A-EGFP with or without 50 ng of pCAG-mCherry using Lipofectamine 3000 (Thermo Fisher Scientific) according to the manufacturer's instructions.

Flow cytometry

At 48 hr after transfection, cells were harvested, washed with phosphate-buffered saline (PBS), and strained into single-cell suspensions using Falcon Round-Bottom Polystyrene Test Tubes with Cell Strainer Snap Caps (Corning). Fluorescence (FITC and PE/Texas Red) was measured using a BD LSRFortessa Cell Analyzer (Roy J. Carver Biotechnology Center Flow

Cytometry Facility, Univ. Illinois). A total of 20,000 events were recorded for each replicate, and data were analyzed using FlowJo v10 (FlowJo, LLC).

Quantitative PCR

At 48 hr after transfection, RNA was extracted from cells using the PureLink RNA Mini Kit (Invitrogen) and converted to complementary DNA (cDNA) using the iScript cDNA Synthesis Kit (Bio-Rad) according to the manufacturers' instructions. qPCR was conducted using 20-40 ng of cDNA per reaction using iTaq Universal SYBR Green Supermix (Bio-Rad). Measurements for each biological replicate were conducted in technical triplicates using validated primers for ataxin-2[83]. Values were compared to GAPDH, and the average fold change was calculated using the $2^{\Delta\Delta CT}$ method. All primer sequences are provided in **Supplementary Table 1**.

Mouse tissues from injected animals were dissected and RNA was extracted and analyzed by qPCR as described above for ataxin-2. hTDP-43 mRNA was measured using the PrimeTime Gene Expression Master Mix (IDT) with the following TaqMan probes: human TDP-43 (Hs00606522_m1; ThermoFisher Scientific) and mouse Actb (Mm02619580_g1; ThermoFisher Scientific).

SG assays

For SGs induced by sorbitol, HEK293T cells were transfected with 1 μg of pAAV-CAG-RfxCas13d-U6-crRNA, pAAV-HiFi-RfxCas13d-U6-crRNA, or pAAV-DiCas7-11-U6-crRNA. At 24 hr post-transfection, cells were transferred to poly-D lysine-coated coverslips (Electron Microscopy Sciences) where, after another 24 hr, they were then incubated with 0.4 M sorbitol

(Sigma-Aldrich) at 37°C for 1 hr. Cells were then fixed with chilled 100% methanol (v/v) for 10 min at RT and subsequently washed twice with PBS.

For assays involving mutant forms of hTDP-43, HEK293T cells were transfected with 800 ng of pAAV-CAG-RfxCas13d-U6-crRNA, pAAV-HiFi-RfxCas13d-U6-crRNA, or pAAV-DiCas7-11-U6-crRNA with 200 ng of pcDNA3.2-hTDP-43^{A315T}-YFP, pcDNA3.2-hTDP-43^{M337V}-YFP or pcDNA3.2-hTDP-43^{G298S}-YFP. At 24 hr after transfection, cells were transferred to poly-D lysine-coated coverslips (Electron Microscopy Sciences) and allowed to adhere. After another 24 hr, cells were then fixed with chilled 100% methanol (v/v) for 10 min at RT and then washed with twice with PBS.

To image SGs, fixed cells were incubated with blocking solution [10% (v/v) donkey serum (Abcam) and 0.1% Triton X-100] for 1 hr at RT and then stained with primary antibody in blocking solution for 1 hr at RT. Cells were then washed three times with PBS and incubated with secondary antibody for 1 hr at RT. Following the incubation, coverslips were washed three times with PBS and mounted onto slides using VECTASHIELD HardSet Antifade Mounting Medium (Vector Laboratories).

Slides were imaged using a Leica TCS SP8 confocal microscope and a Zeiss Observer Z1 microscope (both at the Beckman Institute for Advanced Science and Technology, Univ. Illinois) and an AxioScan.Z1 (Carl R. Woese Institute for Genomic Biology, Univ. Illinois). Image analysis was performed using CellProfiler software as described below.

The following primary antibodies were used: rabbit anti-G3BPI (1:500; MLB International, RN048PW), mouse anti-TDP-43 (1:100; Abnova, H00023435-M01), chicken anti-HA (1:400; Abcam, ab9111).

The following secondary antibodies were used: donkey anti-rabbit Cy3 (1:400; Jackson ImmunoResearch, 711-165-152), donkey anti-mouse Alexa Fluor 488 (1:200; Jackson ImmunoResearch, 715-545-150), donkey anti-chicken Alexa Fluor 647 (1:400; Jackson ImmunoResearch, 703-605-155).

Injections

All animal procedures were approved by the Illinois Institutional Animal Care and Use Committee (IACUC) at the University of Illinois and conducted in accordance with the National Institutes of Health Guide for the Care and Use of Laboratory Animals.

Transgenic TAR4/4 mice were generated by breeding male and female hemizygous TDP-43 mice (B6;SJL-Tg(Thy1-TARDBP)4Singh/J; Jackson Laboratory, Stock No. 012836). Homozygosity was determined by PCR using genomic DNA purified from toe clips. The PCR reaction was conducted using repliQa HiFi ToughMix (Quantabio) using primers (**Supplementary Table 1)** and procedures developed by the Jackson Laboratory. Background-matching mice were generated by breeding male and female B6SJLF1/J mice (B6SJLF1/J; Jackson Laboratory, Stock No. 100012).

ICV and IV injections were conducted on postnatal (P) day 1 or 2 TAR4/4 mice or B6SJLF1/J mice, as described[68]. Briefly, for ICV injections, pups were infused via each lateral ventricle with 4.2 x 10^{10} vg of AAV9-CBh-RfxCas13d-mATXN2 or AAV9-CBh-RfxCas13d-NTG in up to 2 µL of saline using a 10 µL Hamilton syringe with a 30-gauge needle. For IV injections, pups were infused via the facial vein with 7 x 10^{11} vg of AAV9-CBh-RfxCas13d-mATXN2 or AAV9-CBh-RfxCas13d-NTG in up to 50 µL of saline using a 100 µL Hamilton syringe with a 33-gauge needle.

AAV vectors were manufactured by Vector Biolabs.

Behavior

All measurements and scoring were performed by a blinded investigator as described before[26,65]. Gait, kyphosis, and tremors were analyzed daily beginning at P14. Gait impairment was scored as follows: (0) mice show no impairment; (1) mouse has a limp while walking; (2) mouse has either a severe limp, a lowered pelvis, or point feet their away from their body while walking; (3) mouse has either difficulty moving forward, shows minimal joint movement, does not use its feet to generate forward motion, has difficulty staying upright, or drags its abdomen on the ground; (4) mouse has reached end-stage. Mice were euthanized once they scored a 3 for the first time.

Kyphosis was scored as follows: (0) mouse has the ability to straighten spine when walking; (1) mouse has mild curvature of the spine but has the ability to straighten it, (2) mouse has mild curvature of the spine but do does not have the ability to fully straighten it; (3) mouse has a curvature of the spine that is maintained while walking or sitting; (4) mouse has reached end-stage. Mice were euthanized once they scored a 3 for the first time.

Tremor was scored as follows: (0) not observed; (1) mild tremor while moving; (2) severe tremor while moving; (3) severe tremor at rest and while moving; (4) mouse has reached end-stage. Mice were euthanized once they scored a 3 for the first time.

Motor coordination and grip strength were measured every two days beginning at P18. Motor function was determined using an accelerating Rotamex-5 (Columbus Instruments). Briefly, animals were placed on a gradually accelerating apparatus (2.5 RPM to 25 RPM over 115 s) and the average RPM achieved before falling was recorded for each mouse during a three-trial session.

Grip strength was measured using a Grip Strength Meter (Harvard Apparatus). Mice were scruffed and put in position to firmly latch onto a pull bar with their forelimbs and then pulled in the opposite direction. The average maximum force (Newtons) exerted by each animal before their release of the bar was recorded in three-trial sessions. Animals that reached end-stage received a 0 score for rotarod and grip strength.

Kaplan-Meier survival analysis was conducted using the artificial end-points for each animal, which was determined when: (1) animals reached a score of 3 for gait, tremor, or kyphosis, (2) animals were unable to right themselves within 10 sec of being placed on their back, or (3) animals lost 20% of their peak weight.

Immunohistochemistry

Brain and spinal cord were harvested following a transcardial perfusion with PBS. Tissues were subsequently fixed with 4% paraformaldehyde (v/v) at 4°C and sliced into 40-μm sagittal and axial sections using a CM3050 S cryostat (Leica).

Tissue sections were washed three times with PBS and incubated in blocking solution [PBS with 10% (v/v) donkey serum (Abcam) and 1% Triton X-100] for 2 hr at RT and stained with primary antibodies in blocking solution for 72 hr at 4°C. Sections were then washed three times with PBS and incubated with secondary antibodies in blocking solution for 2 hr at RT. Following the incubation with the secondary antibodies, sections were washed three times with PBS and then mounted onto slides using VECTASHIELD HardSet Antifade Mounting Medium (Vector Laboratories). Slides were imaged using a Leica TCS SP8 confocal microscope (Beckman Institute for Advanced Science and Technology, Univ. Illinois) and an AxioScan.Z1 (Carl R. Woese

Institute for Genomic Biology, Univ. Illinois). Image analysis was performed using CellProfiler software and Zeiss ZEN lite software.

The following primary antibodies were used: rabbit anti-HA (1:500, Cell Signaling Technology, C29P4), chicken anti-GFAP (1:1000, Abcam, ab4647), goat anti-Iba1 (1:800, NOVUS, NB100-1028SS), mouse anti-NeuN (1:500, EMD Millipore Corp, MAB377), mouse anti-pTDP-43 (1:3000, CosmoBio, ps409/410), chicken anti-NeuN (1:500, EMD Millipore Corp, ABN91).

The following secondary antibodies were used: donkey anti-rabbit Cy3 (1:200, Jackson ImmunoResearch, 711-165-152), donkey anti-mouse Alexa Fluor 488 (1:125, Jackson ImmunoResearch, 715-545-150), donkey anti-chicken Alexa Fluor 647 (1:125, Jackson ImmunoResearch, 703-605-155), donkey anti-goat Alexa Fluor 647 (1:200, Jackson ImmunoResearch, 705-605-147).

Image analysis

Quantification of cell numbers, inclusion counts and inclusion size were performed using CellProfiler 4.2.1 (Broad Institute, Cambridge, MA)[84]. All imaging was performed by a blinded investigator and the same pipeline was used to analyze all condition(s) and/or group(s) from the same experiment.

Parameters for cell and inclusion size, as well as the thresholding and filtering methods were executed as described[85]. Briefly, cells were first identified using the Identify Primary Objects module. For sorbitol-treated cells, individual cells were identified by TDP-43 immunostaining using a global, two-class Otsu thresholding method. For cells transfected with the hTDP-43-YFP reporter plasmid, cells were identified by HA immunostaining using the global, robust background

thresholding method. The shape of the cells was then used to distinguish clumped objects and to draw dividing lines between them. Cell diameter setting were 50 to 180 pixels for sorbitol-treated cells, 50 to 150 pixels for TDP-43^{A315T}, and 60 to 180 pixels for TDP-43^{M337V} and TDP-43^{G298S}.

Prior to quantifying inclusions, images were filtered to enhance foci. Then, to find inclusions, the Identify Primary Objects module was used to distinguish clumped objects by foci intensity. For sorbitol-treated cells, inclusions were identified using the global, two-class Otsu thresholding method and a thresholding correction factor of 5. The diameter range used to identify foci was 3 to 25 pixels for TDP-43^{+} inclusions and 1 to 35 for G3BPI^{+} SGs. Then, the Relate Objects module was used to colocalize G3BPI^{+} SGs and TDP-43^{+} inclusions, which were in turn mapped to their respective cells to quantify the number of cells carrying foci for both G3BPI and TDP-43. This number was divided by the total number of analyzed cells to determine the percentage of cells with G3BPI^{+} and TDP-43^{+} foci.

To identify YFP^{+} inclusions, the global, two-class Otsu thresholding method was used for TDP-43^{A315T} using a diameter range of 5 to 35 pixels. For TDP-43^{M337V} and TDP-43^{G298S} conditions, the global, robust background thresholding method was used to identify YFP^{+} inclusions in the range of 5 to 40 pixels. Once identified, inclusions were mapped to each cell using the Relate Objects module and the number inclusions per cell and the area occupied by inclusions were determined.

To quantify images from tissue sections, cells were identified using the Identify Primary Objects module with the global, two-class Otsu thresholding method for GFAP^{+}, NeuN^{+} and soluble pTDP-43^{+} immunostaining or the global, robust background thresholding method for Iba1^{+} and HA^{+} cells. Cells identified by HA were mapped to NeuN^{+} cells using the Relate Objects module to find the percentage of HA^{+} neurons. Similarly, cells identified to express soluble pTDP-

43 were mapped to NeuN$^+$ cells using the Relate Objects module to find the percentage of soluble pTDP-43$^+$ neurons out of all NeuN$^+$ cells analyzed.

To identify inclusions exclusively in NeuN$^+$ cells, objects identified as neurons were used as a mask for the pTDP-43 and ubiquitin immunostaining. Prior to quantifying inclusions, images were filtered to enhance foci. Then, to find inclusions, the Identify Primary Objects module was used with the global two-class Otsu thresholding method using foci intensity to distinguish clumped objects. The number of foci per image was quantified and this number divided by the total number of NeuN+ cells identified.

RNA sequencing

Library construction was performed by the Roy J. Carver Biotechnology Center (Univ. Illinois) as previously described[47]. Briefly, libraries were prepared with the Kapa Hyper Stranded mRNA library kit (Roche), quantitated by qPCR, pooled, and sequenced on two SP lanes for 101 cycles from one end of the fragments on a NovaSeq 6000 with V1.5 sequencing kits. FASTQ files were generated and demultiplexed with the bcl2fastq v2.20 Conversion Software (Illumina). The quality of the demultiplexed FastQ files was evaluated using FastQC (version 0.11.8). Average per-base read quality scores were high quality (over 30 in all samples) and no adapter sequences were found.

RNA-seq analysis was conducted by the High-Performance Biological Computing Core (Univ. Illinois) as previously described[47]. Salmon3 version 1.5.2 was used to quasi-map reads to the transcriptome and to quantify the abundance of each transcript. Transcriptomes were indexed using the decoy-aware method in Salmon with the entire *Mus musculus* transcriptome file (GCF_000001635.27_GRCm39_genomic.fna) from NCBI FTP site as the decoy sequence. Then

quasi-mapping was performed to map reads to the transcriptome with additional arguments: --seqBias and --gcBias were used to correct sequence- and GC-specific biases, --numBootstraps=30 was used to compute bootstrap transcript abundance estimates and --validateMappings and --recoverOrphans were used to improve the accuracy of mappings.

Gene-level counts were estimated based on transcript-level counts using the "lengthScaledTPM" method from the tximport package to provide accurate gene-level counts estimates and to keep multi-mapped reads in the analysis. Differential gene expression (DEG) analysis was performed using the limma-trend method using a model of Trt factor. A linear model was fit to find the relationship between the gene expression and Trt variable for pairwise comparisons between groups. The limma package was utilized to estimate raw P-values and False Discovery Rate (FDR) corrected P-values for the DEG analysis. RNA-seq data is available in **Supplementary File** 1.

Statistical analysis

Statistical analysis was performed using GraphPad Prism 9. For *in vitro* studies, mATXN2-T2A-EGFP fluorescence intensity, mCherry fluorescence intensity, TDP-YFP fluorescence intensity, ATXN2 mRNA, as well as inclusion size, number and percentages were compared using an unpaired one-tailed t-test. For *in vivo* studies, ataxin-2 mRNA, hTDP-43 mRNA, and the percentage of neurons expressing soluble pTDP-43 were compared using an unpaired one-tailed t-test; gait impairment and grip strength were analyzed by two-way analysis of variance (ANOVA); kyphosis, tremor, and weight were analyzed by a mixed effects model; rotarod was compared using an unpaired one-tailed *t*-test. Survival was analyzed by Kaplan-Meier analyses using the Mantel-Cox test.

ACKNOWLEDGMENTS

This work was supported by the NIH/NINDS (1U01NS122102-01A1 and 1R01NS123556-01A1), the NIH/NIGMS (5R01GM141296), the Muscular Dystrophy Association (MDA602798), the Simons Foundation (887187), the Parkinson's Disease Foundation (PF-IMP-1950) and the Judith & Jean Pape Adams Foundation. M.A.Z.C. was supported by the NIH/NIBIB (T32EB019944), the Mavis Future Faculty Fellows Program, and a Aspire Fellowship from the University of Illinois Urbana-Champaign. T.S. was supported by a Summer Undergraduate Research Fellowship from the School of Molecular & Cellular Biology at the University of Illinois Urbana-Champaign.

AUTHOR CONTRUBUTIONS

T.G. and M.A.Z.C. conceived of the study. M.A.Z.C. and S.Z. designed and cloned the plasmids. M.A.Z.C. and S.Z. conducted flow cytometry. M.A.Z.C. and H.J.M. conducted qPCR measurements. M.A.Z.C. conducted immunocytochemistry. M.A.Z.C., J.E.P. and H.J.M. bred and genotyped animals. M.A.Z.C. and J.E.P. performed injections. H.J.M. conducted behavior measurements as a blinded investigator. M.A.Z.C. and H.J.M. harvested and dissected tissues. M.A.Z.C., H.J.M. and T.J.S. sectioned tissue and conducted immunohistochemistry. M.A.Z.C. and T.J.S. acquired images. M.A.Z.C. and T.J.S. created pipelines for image analysis. T.G. and M.A.Z.C. wrote the manuscript with input from all authors.

COMPETING INTEREST

T.G. and J.P. previously filed a patent application on technologies used in this manuscript. The authors have no other competing interests to disclose.

REFERENCES

1. Ling, S.-C., Polymenidou, M. & Cleveland, D. W. Converging mechanisms in ALS and FTD: Disrupted RNA and protein homeostasis. *Neuron* **79**, 416–438 (2013).

2. Neumann, M. *et al.* Ubiquitinated TDP-43 in frontotemporal lobar degeneration and amyotrophic lateral sclerosis. *Science* **314**, 130–133 (2006).

3. Mackenzie, I. R. A. *et al.* Pathological TDP-43 distinguishes sporadic amyotrophic lateral sclerosis from amyotrophic lateral sclerosis withSOD1 mutations. *Ann. Neurol.* **61**, 427–434 (2007).

4. Arai, T. *et al.* TDP-43 is a component of ubiquitin-positive tau-negative inclusions in frontotemporal lobar degeneration and amyotrophic lateral sclerosis. *Biochem. Biophys. Res. Commun.* **351**, 602–611 (2006).

5. Lagier-Tourenne, C. & Cleveland, D. W. Rethinking ALS: The FUS about TDP-43. *Cell* **136**, 1001–1004 (2009).

6. Mackenzie, I. R. A. & H. Feldman, H. Ubiquitin immunohistochemistry suggests classic motor neuron disease, motor neuron disease with dementia, and frontotemporal dementia of the motor neuron disease type represent a clinicopathologic spectrum: *J. Neuropathol. Exp. Neurol.* **64**, 730–739 (2005).

7. Rowland, L. P. & Shneider, N. A. Amyotrophic lateral sclerosis. *N. Engl. J. Med.* **344**, 1688–1700 (2001).

8. Polymenidou, M. *et al.* Long pre-mRNA depletion and RNA missplicing contribute to neuronal vulnerability from loss of TDP-43. *Nat. Neurosci.* **14**, 459–468 (2011).

9. Johnson, B. S., McCaffery, J. M., Lindquist, S. & Gitler, A. D. A yeast TDP-43 proteinopathy model: Exploring the molecular determinants of TDP-43 aggregation and cellular toxicity. *Proc. Natl. Acad. Sci.* **105**, 6439–6444 (2008).

10. Winton, M. J. *et al.* Disturbance of nuclear and cytoplasmic TAR DNA-binding protein (TDP-43) induces disease-like redistribution, sequestration, and aggregate formation. *J. Biol. Chem.* **283**, 13302–13309 (2008).

11. Pesiridis, G. S., Lee, V. M.-Y. & Trojanowski, J. Q. Mutations in TDP-43 link glycine-rich domain functions to amyotrophic lateral sclerosis. *Hum. Mol. Genet.* **18**, R156–R162 (2009).

12. Sreedharan, J. *et al.* TDP-43 mutations in familial and sporadic amyotrophic lateral sclerosis. *Science* **319**, 1668–1672 (2008).

13. Kovacs, G. G. *et al. TARDBP* variation associated with frontotemporal dementia, supranuclear gaze palsy, and chorea: *TARDBP* Variation and Frontotemporal Dementia. *Mov. Disord.* **24**, 1842–1847 (2009).

14. Benajiba, L. *et al. TARDBP* mutations in motoneuron disease with frontotemporal lobar degeneration. *Ann. Neurol.* **65**, 470–473 (2009).

15. Cohen, T. J., Lee, V. M. Y. & Trojanowski, J. Q. TDP-43 functions and pathogenic mechanisms implicated in TDP-43 proteinopathies. *Trends Mol. Med.* **17**, 659–667 (2011).

16. Kraemer, B. C. *et al.* Loss of murine TDP-43 disrupts motor function and plays an essential role in embryogenesis. *Acta Neuropathol. (Berl.)* **119**, 409–419 (2010).

17. Feiguin, F. *et al.* Depletion of TDP-43 affects *Drosophila motoneurons* terminal synapsis and locomotive behavior. *FEBS Lett.* **583**, 1586–1592 (2009).

18. Yang, C. *et al.* Partial loss of TDP-43 function causes phenotypes of amyotrophic lateral sclerosis. *Proc. Natl. Acad. Sci.* **111**, (2014).

19. Herzog, J. J., Deshpande, M., Shapiro, L., Rodal, A. A. & Paradis, S. TDP-43 misexpression causes defects in dendritic growth. *Sci. Rep.* **7**, 15656 (2017).

20. Elden, A. C. *et al.* Ataxin-2 intermediate-length polyglutamine expansions are associated with increased risk for ALS. *Nature* **466**, 1069–1075 (2010).

21. Hayes, L. R. & Kalab, P. Emerging therapies and novel targets for TDP-43 proteinopathy in ALS/FTD. *Neurotherapeutics* **19**, 1061–1084 (2022).

22. Armakola, M. *et al.* Inhibition of RNA lariat debranching enzyme suppresses TDP-43 toxicity in ALS disease models. *Nat. Genet.* **44**, 1302–1309 (2012).

23. Kim, H.-J. *et al.* Therapeutic modulation of eIF2α phosphorylation rescues TDP-43 toxicity in amyotrophic lateral sclerosis disease models. *Nat. Genet.* **46**, 152–160 (2014).

24. Couthouis, J. *et al.* A yeast functional screen predicts new candidate ALS disease genes. *Proc. Natl. Acad. Sci.* **108**, 20881–20890 (2011).

25. Nihei, Y., Ito, D. & Suzuki, N. Roles of ataxin-2 in pathological cascades mediated by TAR DNA-binding protein 43 (TDP-43) and fused in sarcoma (FUS). *J. Biol. Chem.* **287**, 41310–41323 (2012).

26. Becker, L. A. *et al.* Therapeutic reduction of ataxin-2 extends lifespan and reduces pathology in TDP-43 mice. *Nature* **544**, 367–371 (2017).

27. Satterfield, T. F. & Pallanck, L. J. Ataxin-2 and its Drosophila homolog, ATX2, physically assemble with polyribosomes. *Hum. Mol. Genet.* **15**, 2523–2532 (2006).

28. Lee, T. *et al.* Ataxin-2 intermediate-length polyglutamine expansions in European ALS patients. *Hum. Mol. Genet.* **20**, 1697–1700 (2011).

29. Ross, O. A. *et al.* Ataxin-2 repeat-length variation and neurodegeneration. *Hum. Mol. Genet.* **20**, 3207–3212 (2011).

30. Daoud, H. *et al.* Association of long ATXN2 CAG repeat sizes with increased risk of amyotrophic lateral sclerosis. *Arch. Neurol.* **68**, (2011).

31. Chen, Y. *et al.* Ataxin-2 intermediate-length polyglutamine: a possible risk factor for Chinese patients with amyotrophic lateral sclerosis. *Neurobiol. Aging* **32**, 1925.e1-1925.e5 (2011).

32. Van Langenhove, T. *et al.* Ataxin-2 polyQ expansions in FTLD-ALS spectrum disorders in Flanders-Belgian cohorts. *Neurobiol. Aging* **33**, 1004.e17-1004.e20 (2012).

33. Jinek, M. *et al.* A programmable dual-RNA–guided DNA endonuclease in adaptive bacterial immunity. *Science* **337**, 816–821 (2012).

34. Cong, L. *et al.* Multiplex genome engineering using CRISPR/Cas systems. *Science* **339**, 819–823 (2013).

35. Sander, J. D. & Joung, J. K. CRISPR-Cas systems for editing, regulating and targeting genomes. *Nat. Biotechnol.* **32**, 347–355 (2014).

36. Abudayyeh, O. O. *et al.* RNA targeting with CRISPR–Cas13. *Nature* **550**, 280–284 (2017).

37. Abudayyeh, O. O. *et al.* C2c2 is a single-component programmable RNA-guided RNA-targeting CRISPR effector. *Science* **353**, aaf5573 (2016).

38. Cox, D. B. T. *et al.* RNA editing with CRISPR-Cas13. *Science* **358**, 1019–1027 (2017).

39. Smargon, A. A. *et al.* Cas13b is a type VI-B CRISPR-associated RNA-guided RNase differentially regulated by accessory proteins Csx27 and Csx28. *Mol. Cell* **65**, 618-630.e7 (2017).

40. Yan, W. X. *et al.* Cas13d is a compact RNA-targeting type VI CRISPR effector positively modulated by a WYL-domain-containing accessory protein. *Mol. Cell* **70**, 327-339.e5 (2018).

41. Konermann, S. *et al.* Transcriptome engineering with RNA-targeting type VI-D CRISPR effectors. *Cell* **173**, 665-676.e14 (2018).

42. East-Seletsky, A. *et al.* Two distinct RNase activities of CRISPR-C2c2 enable guide-RNA processing and RNA detection. *Nature* **538**, 270–273 (2016).

43. Özcan, A. *et al.* Programmable RNA targeting with the single-protein CRISPR effector Cas7-11. *Nature* **597**, 720–725 (2021).

44. Dewey, C. M. *et al.* TDP-43 is directed to stress granules by sorbitol, a novel physiological osmotic and oxidative stressor. *Mol. Cell. Biol.* **31**, 1098–1108 (2011).

45. Mackenzie, I. R. *et al.* TIA1 Mutations in amyotrophic lateral sclerosis and frontotemporal dementia promote phase separation and alter stress granule dynamics. *Neuron* **95**, 808-816.e9 (2017).

46. Boeynaems, S. *et al.* Phase separation of C9orf72 dipeptide repeats perturbs stress granule dynamics. *Mol. Cell* **65**, 1044-1055.e5 (2017).

47. Powell, J. E. *et al.* Targeted gene silencing in the nervous system with CRISPR-Cas13. *Sci. Adv.* **8**, eabk2485 (2022).

48. Guo, Y. *et al.* Specific knockdown of Htra2 by CRISPR-CasRx prevents acquired sensorineural hearing loss in mice. *Mol. Ther. Nucleic Acids* **28**, 643–655 (2022).

49. Morelli, K. H. *et al.* An RNA-targeting CRISPR–Cas13d system alleviates disease-related phenotypes in Huntington's disease models. *Nat. Neurosci.* **26**, 27–38 (2023).

50. Ai, Y., Liang, D. & Wilusz, J. E. CRISPR/Cas13 effectors have differing extents of off-target effects that limit their utility in eukaryotic cells. *Nucleic Acids Res.* **50**, e65–e65 (2022).

51. Kelley, C. P., Haerle, M. C. & Wang, E. T. Negative autoregulation mitigates collateral RNase activity of repeat-targeting CRISPR-Cas13d in mammalian cells. *Cell Rep.* **40**, 111226 (2022).

52. Li, Y. *et al.* The collateral activity of RfxCas13d can induce lethality in a RfxCas13d knock-in mouse model. *Genome Biol.* **24**, 20 (2023).

53. Shi, P. *et al.* Collateral activity of the CRISPR/RfxCas13d system in human cells. *Commun. Biol.* **6**, 334 (2023).

54. Wang, Q. *et al.* The CRISPR-Cas13a gene-editing system induces collateral cleavage of RNA in glioma cells. *Adv. Sci.* **6**, 1901299 (2019).

55. Nonhoff, U. *et al.* Ataxin-2 interacts with the DEAD/H-box RNA helicase DDX6 and interferes with P-bodies and stress granules. *Mol. Biol. Cell* **18**, 1385–1396 (2007).

56. Colombrita, C. *et al.* TDP-43 is recruited to stress granules in conditions of oxidative insult. *J. Neurochem.* **111**, 1051–1061 (2009).

57. Parker, S. J. *et al.* Endogenous TDP-43 localized to stress granules can subsequently form protein aggregates. *Neurochem. Int.* **60**, 415–424 (2012).

58. Liu-Yesucevitz, L. *et al.* Tar DNA binding protein-43 (TDP-43) associates with stress granules: analysis of cultured cells and pathological brain tissue. *PLoS ONE* **5**, e13250 (2010).

59. Dewey, C. M. *et al.* TDP-43 aggregation in neurodegeneration: are stress granules the key? *Brain Res.* **1462**, 16–25 (2012).

60. Sidibé, H. *et al.* TDP-43 stabilizes *G3BP1* mRNA: relevance to amyotrophic lateral sclerosis/frontotemporal dementia. *Brain* **144**, 3461–3476 (2021).

61. Liu-Yesucevitz, L. *et al.* ALS-linked mutations enlarge TDP-43-enriched neuronal RNA granules in the dendritic arbor. *J. Neurosci.* **34**, 4167–4174 (2014).

62. Ling, S.-C. *et al.* ALS-associated mutations in TDP-43 increase its stability and promote TDP-43 complexes with FUS/TLS. *Proc. Natl. Acad. Sci.* **107**, 13318–13323 (2010).

63. Corcia, P. *et al.* Phenotype and genotype analysis in amyotrophic lateral sclerosis with TARDBP gene mutations. *Neurology* **78**, 1519–1526 (2012).

64. Barmada, S. J. *et al.* Cytoplasmic mislocalization of TDP-43 is toxic to neurons and enhanced by a mutation associated with familial amyotrophic lateral sclerosis. *J. Neurosci.* **30**, 639–649 (2010).

65. Wils, H. *et al.* TDP-43 transgenic mice develop spastic paralysis and neuronal inclusions characteristic of ALS and frontotemporal lobar degeneration. *Proc. Natl. Acad. Sci.* **107**, 3858–3863 (2010).

66. Foust, K. D. *et al.* Intravascular AAV9 preferentially targets neonatal neurons and adult astrocytes. *Nat. Biotechnol.* **27**, 59–65 (2009).

67. Chakrabarty, P. *et al.* Capsid serotype and timing of injection determines AAV transduction in the neonatal mice brain. *PLoS ONE* **8**, e67680 (2013).

68. Di Meo, I., Marchet, S., Lamperti, C., Zeviani, M. & Viscomi, C. AAV9-based gene therapy partially ameliorates the clinical phenotype of a mouse model of Leigh syndrome. *Gene Ther.* **24**, 661–667 (2017).

69. Armbruster, N. *et al.* Efficacy and biodistribution analysis of intracerebroventricular administration of an optimized scAAV9-SMN1 vector in a mouse model of spinal muscular atrophy. *Mol. Ther. - Methods Clin. Dev.* **3**, 16060 (2016).

70. Corrà, S., Cerutti, R., Balmaceda, V., Viscomi, C. & Zeviani, M. Double administration of self-complementary AAV9 *NDUFS4* prevents Leigh disease in *Ndufs4* −/− mice. *Brain* **145**, 3405–3414 (2022).

71. Inukai, Y. *et al.* Abnormal phosphorylation of Ser409/410 of TDP-43 in FTLD-U and ALS. *FEBS Lett.* **582**, 2899–2904 (2008).

72. Tong, H. *et al.* High-fidelity Cas13 variants for targeted RNA degradation with minimal collateral effects. *Nat. Biotechnol.* (2022) doi:10.1038/s41587-022-01419-7.

73. Zheng, Z. *et al.* Preventing autosomal-dominant hearing loss in Bth mice with CRISPR/CasRx-based RNA editing. *Signal Transduct. Target. Ther.* **7**, 79 (2022).

74. Smith, R. A. Antisense oligonucleotide therapy for neurodegenerative disease. *J. Clin. Invest.* **116**, 2290–2296 (2006).

75. Foust, K. D. *et al.* Therapeutic AAV9-mediated suppression of mutant SOD1 slows disease progression and extends survival in models of inherited ALS. *Mol. Ther.* **21**, 2148–2159 (2013).

76. Lim, C. K. W. *et al.* Treatment of a mouse model of ALS by in vivo base editing. *Mol. Ther.* **28**, 1177–1189 (2020).

77. Lagier-Tourenne, C. *et al.* Targeted degradation of sense and antisense *C9orf72* RNA foci as therapy for ALS and frontotemporal degeneration. *Proc. Natl. Acad. Sci.* **110**, (2013).

78. Meijboom, K. E. *et al.* CRISPR/Cas9-mediated excision of ALS/FTD-causing hexanucleotide repeat expansion in C9ORF72 rescues major disease mechanisms in vivo and in vitro. *Nat. Commun.* **13**, 6286 (2022).

79. Tran, H. *et al.* Suppression of mutant C9orf72 expression by a potent mixed backbone antisense oligonucleotide. *Nat. Med.* **28**, 117–124 (2022).

80. Zeballos C., M. A. & Gaj, T. Next-generation CRISPR technologies and their applications in gene and cell therapy. *Trends Biotechnol.* **39**, 692–705 (2021).

81. Gray, S. J. *et al.* Optimizing promoters for recombinant adeno-associated virus-mediated gene expression in the peripheral and central nervous system using self-complementary vectors. *Hum. Gene Ther.* **22**, 1143–1153 (2011).

82. Powell, S. K., Samulski, R. J. & McCown, T. J. AAV capsid-promoter interactions determine CNS cell-selective gene expression in vivo. *Mol. Ther.* **28**, 1373–1380 (2020).

83. Scoles, D. R. *et al.* Antisense oligonucleotide therapy for spinocerebellar ataxia type 2. *Nature* **544**, 362–366 (2017).

84. Carpenter, A. E. *et al.* CellProfiler: image analysis software for identifying and quantifying cell phenotypes. *Genome Biol.* **7**, R100 (2006).

85. Oyston, L. J. *et al.* Rapid in vitro quantification of TDP-43 and FUS mislocalisation for screening of gene variants implicated in frontotemporal dementia and amyotrophic lateral sclerosis. *Sci. Rep.* **11**, 14881 (2021).

FIGURES

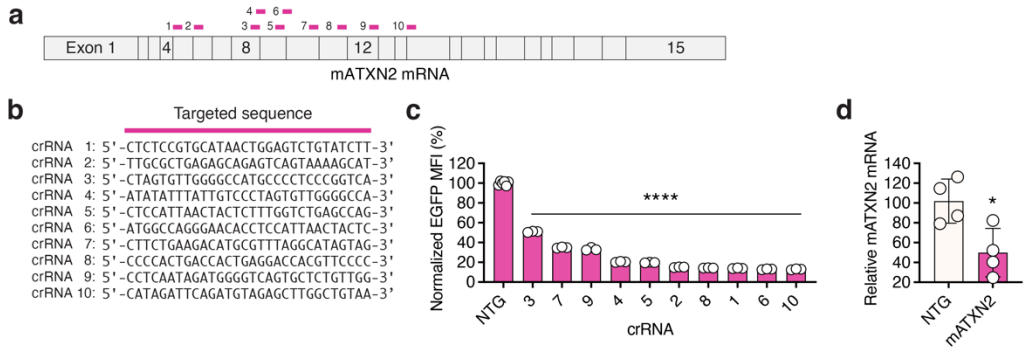

Fig. 1. Programming RfxCas13d to target ataxin-2. (a) Schematic of the mature mouse ataxin-2 (mATXN2) mRNA and location of the crRNA (CRISPR RNA) binding sites (pink bars). **(b)** crRNA sequences targeting mATXN2. **(c)** EGFP mean fluorescence intensity (MFI) in HEK293T cells transfected with mATXN2-T2A-EGFP alongside RfxCas13d and each mATXN2-targeting crRNA. Data are normalized to MFI from cells transfected with mATXN2-T2A-EGFP, RfxCas13d and a non-targeted (NTG) crRNA (n = 3). Values represent means and error bars indicate SD. ****P < 0.0001; one-tailed unpaired *t*-test. **(d)** Relative mATXN2 mRNA from Neuro2A cells transfected with RfxCas13d and crRNA-10. Data are normalized to relative mATXN2 mRNA in cells transfected with RfxCas13d and NTG crRNA (n = 4). Error bars indicate SEM. *P < 0.05; one-tailed unpaired *t*-test.

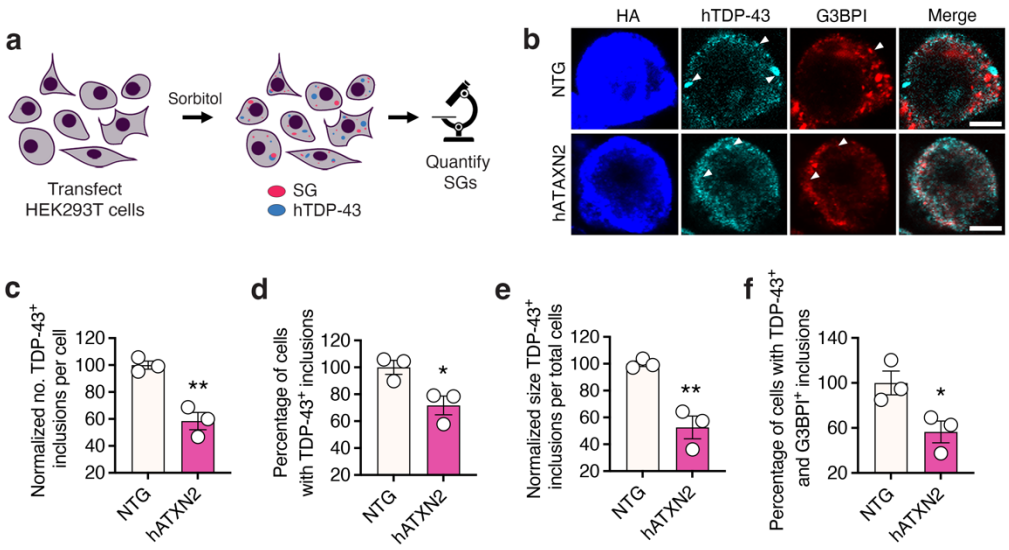

Fig. 2. RfxCas13d targeting reduces TDP-43 aggregation. (a) Workflow for analyzing TDP-43 aggregation. **(b)** Representative immunofluorescent staining of HEK293T cells after transfection with RfxCas13d and crRNA-6 and treatment with sorbitol for 1 hr. HA, hemagglutinin epitope tag; G3BPI, Stress granulate (SG) marker Ras-GAP SH3-domain-binding protein 1. Scale bar, 5 µm. White arrowheads indicate presence or absence of inclusions. Images were captured using identical exposure conditions. **(c, d, e, f)** Quantification of **(c)** the number of TDP-43^{+} foci per individual cell; **(d)** the percentage of cells expressing one or more TDP-43^{+} inclusions; **(e)** the area occupied by TDP-43^{+} foci divided by the number of cells analyzed per image; **(f)** the percentage of cells identified to express inclusions positive for both G3BPI and TDP-43. All data are normalized to cells transfected with RfxCas13d and a NTG crRNA (n = 3). Values represent means and error bars indicate SEM. *P < 0.05; **P < 0.01; one-tailed unpaired *t* test.

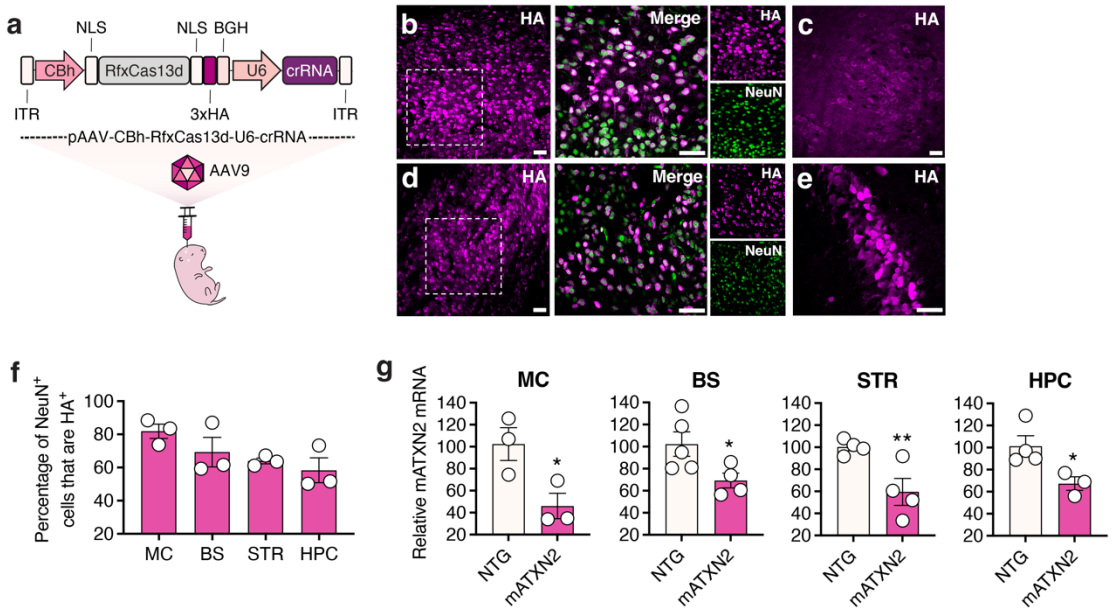

Fig. 3. AAV-mediated delivery of RfxCas13d reduces ATXN2 mRNA in the brain. (a) (Top) Schematic of the AAV vector encoding RfxCas13d and its crRNA**.** (Bottom) Overview of the injections conducted in P1-P2 B6SJLF1/J mice. White stars indicate injection sites. ITR, inverted terminal repeat; CBh, chicken β-actin promoter; NLS, nuclear localization signal; BGH, bovine growth hormone polyadenylation signal. **(b, c, d, e)** Representative immunofluorescence staining of the **(b)** motor cortex (MC), **(c)** brainstem (BC), **(d)** striatum (STR) and **(e)** hippocampus (HPC). Scale bar, 50 µm. **(f)** Quantification of the percentage of $NeuN^+$ cells positive for the HA epitope tag (n = 3). **(g)** Relative mATXN2 mRNA in B6SJLF1/J mice injected with AAV9-CBh-RfxCas13d-mATXN2. Data are normalized to relative mATXN2 mRNA from B6SJLF1/J mice injected with AAV9-CBh-RfxCas13d-NTG. Values represent means and error bars indicate SEM (n = 3 for the MC; n = 5 for NTG and n = 4 for mATXN2 in the BS; n = 4 for the STR; n = 4 for NTG and n = 3 for mATXN2 in the HPC). *$P < 0.05$; **$P < 0.01$; one-tailed unpaired *t*-test. All analyses conducted four weeks post-injection.

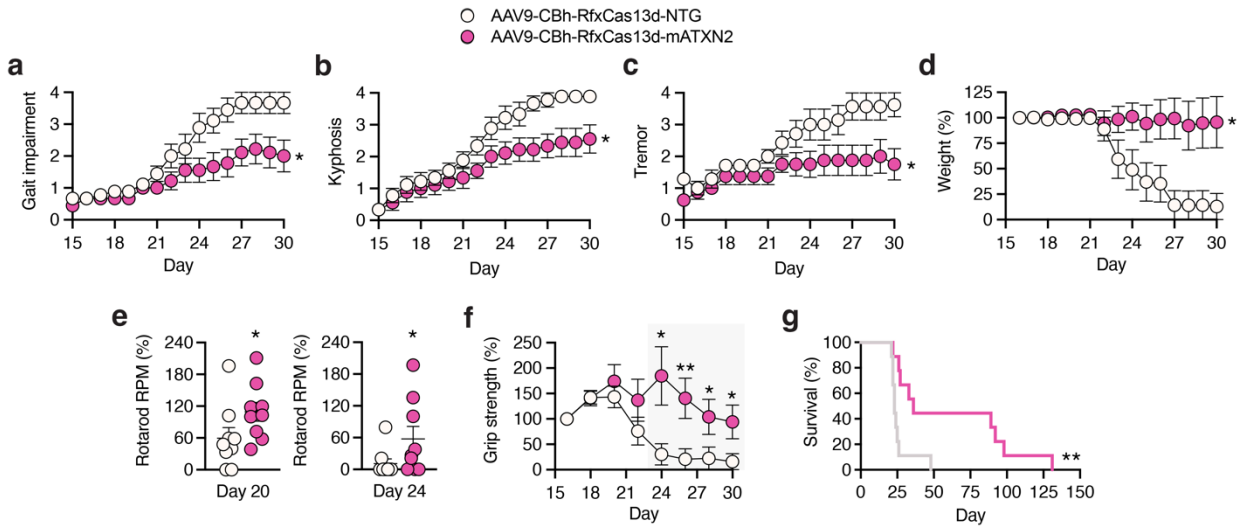

Fig. 4. RfxCas13d improved functional deficits and increased survival in TAR4/4 mice. (a) Gait, **(b)** kyphosis, **(c)** tremor, **(d)** weight, **(e)** rotarod, **(f)** forelimb grip strength and **(g)** percent survival of TAR4/4 mice injected with AAV9-CBh-RfxCas13d-mATXN2 or AAV9-CBh-RfxCas13d-NTG. **(a, b, d, e, f, g)** n = 9 for mATXN2 and n = 9 for NTG; **(c)** n = 8 for mATXN2 and n = 7 for NTG. **(d-f)** Mean values for each mouse normalized to day 16 values for the same subject. **(f)** Values represent means and error bars indicate SEM. *P < 0.05; **P < 0.01. **(a, f)** two-way ANOVA; **(b-d)** mixed-effects model; **(e)** one-tailed unpaired *t*-test; **(g)** Log-rank Mantel-Cox test.

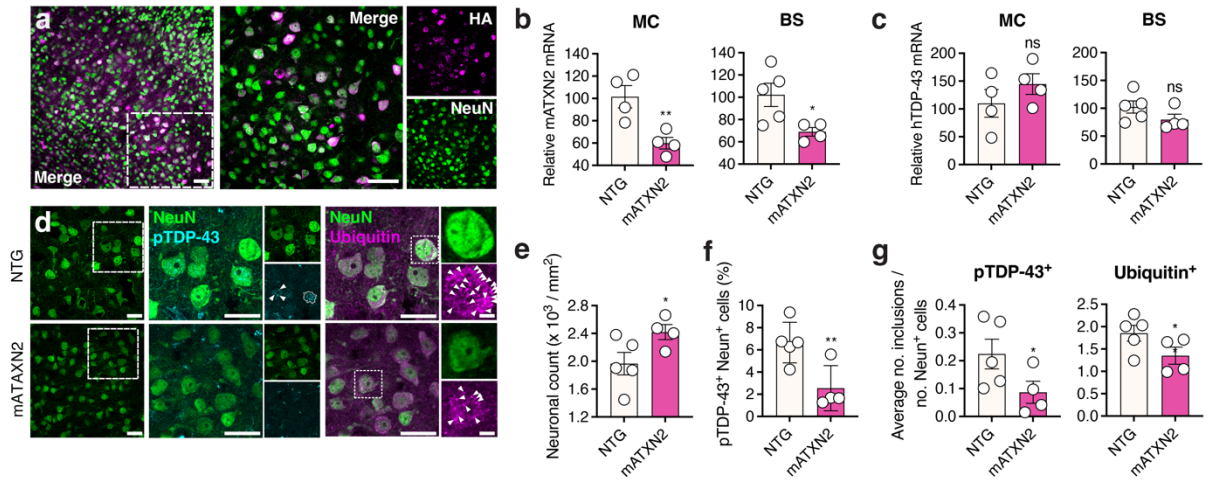

Fig. 5. Targeting ataxin-2 with RfxCas13d reduced the severity of neuropathological hallmarks in TAR4/4 mice. (a) Representative immunofluorescence staining of the motor cortex (MC) in TAR4/4 mice injected with AAV9-CBh-RfxCas13d-mATXN2**.** Relative **(b)** mATXN2 mRNA and (c) hTDP-43 mRNA in the MC and brain stem (BS) from TAR4/4 mice injected with AAV9-CBh-RfxCas13d-mATXN2. Data are normalized to relative mRNA from the MC and BS from mice injected with AAV9-CBh-RfxCas13d-NTG. **(b)** Error bars indicate SEM (n = 4 for the MC: n = 5 for NTG and n = 4 for the mATXN2 for the BS). ns, P > 0.05; *P < 0.05; **P < 0.01; one-tailed unpaired *t*-test. **(d)** Representative immunofluorescence staining of the MC. White arrowheads indicate inclusions and white dotted outlines denote soluble pTDP-43. White box denotes the area presented in the inset. Images were captured using identical exposure conditions. Scale bar, (left) 25 µm and (right) 5 µm. **(e-g)** Quantification of immunofluorescence staining of the MC by CellProfiler. Error bars indicate SEM (n = 5 for NTG and n = 4 for mATXN2). *P < 0.05; **P < 0.01**;** one-tailed unpaired *t*-test. All analysis conducted on end-stage tissues from TAR4/4 mice injected at P1-2.

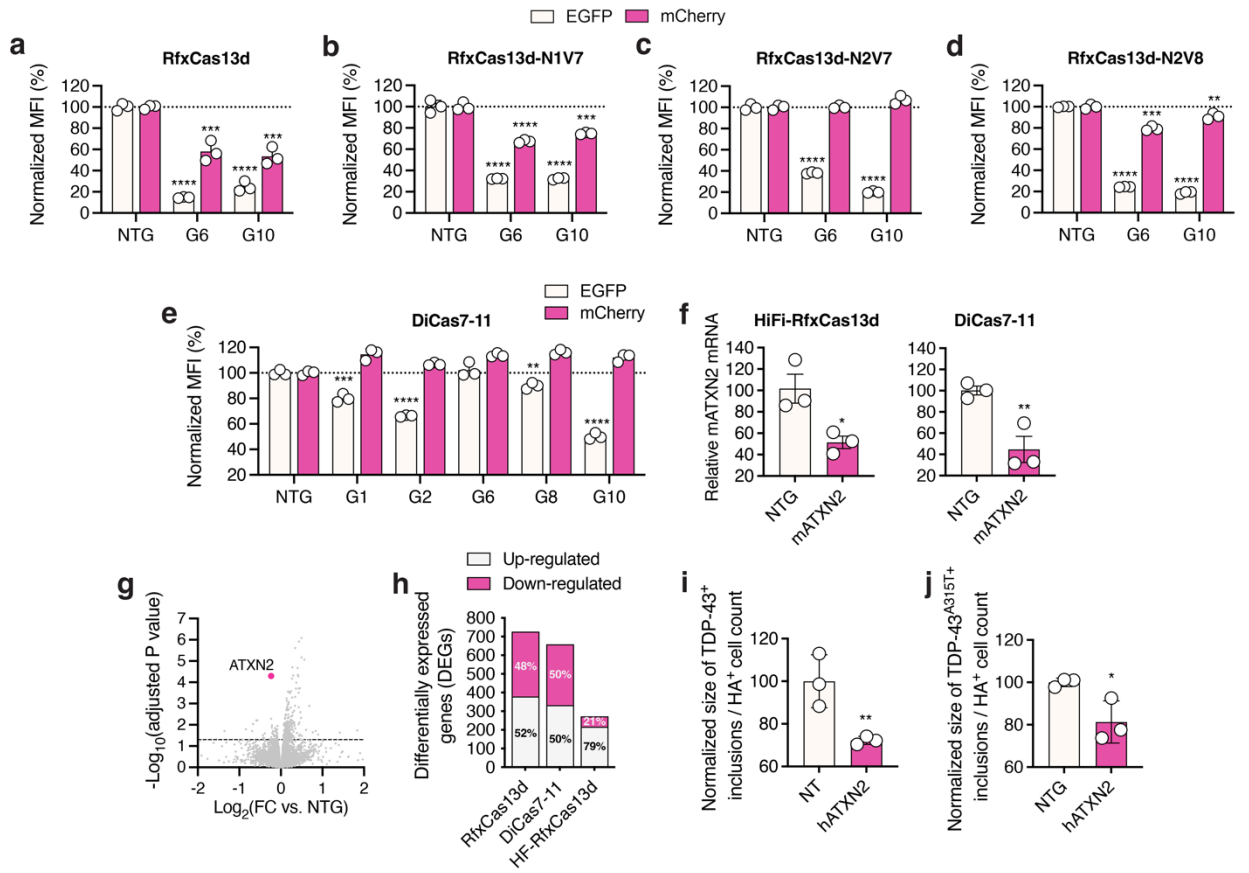

Fig. 6. High-fidelity (HiFi) RfxCas13d and DiCas7-11 can target ataxin-2. (a-e) EGFP and mCherry mean fluorescence intensity (MFI) in HEK293T cells transfected with mATXN2-T2A-EGFP and pCAG-mCherry with an RfxCas13d variant or DiCas7-11 and a mATXN2-targeting crRNA. Data are normalized to MFI from cells transfected with mATXN2-T2A-EGFP and pCAG-mCherry with RfxCas13d or DiCas7-11 and a non-targeted (NTG) crRNA (n = 3). Error bars indicate SD. *P < 0.05; **P < 0.005; ***P < 0.001; ****P < 0.0001; one-tailed unpaired *t*-test. **(f)** Relative mATXN2 mRNA from Neuro2A cells transfected with RfxCas13d-N2V7 (HiFi-RfxCas13d) or DiCas7-11 and crRNA-10. Data are normalized to mATXN2 mRNA from cells transfected with each variant and NTG crRNA (n = 3). Error bars indicate SEM. *P < 0.05; **P < 0.01; one-tailed unpaired *t*-test. **(g)** Volcano plot of RNA-seq data comparing Neuro2A cells transfected with HiFi-RfxCas13d and crRNA-10 to HiFi-RfxCas13d with NTG crRNA (n = 3).

Pink circle indicates mATXN2. Dotted line denotes the cut-off for values with an FDR-adjusted $P < 0.05$. (**h**) Number of differentially expressed genes (DEGs) [>1-fold change (FC), FDR-adjusted P-value < 0.05] in Neuro2A cells transfected with RfxCas13d, HiFi-RfxCas13d or DiCas7-11 with crRNA-10 relative to cells transfected with each variant and NTG crRNA (n = 3). **(i)** Quantification of the immunofluorescent analysis in HEK293T cells their transfection with HiFi-RfxCas13d and crRNA-6 and treatment with sorbitol. Data are normalized to cells transfected with RfxCas13d and a NTG crRNA (n = 3). **(j)** Quantification of the immunofluorescent analysis in HEK293T cells after transfection with YFP-TDP-43^{A315T} and HiFi-RfxCas13d with crRNA-6. Data are normalized to cells transfected with YFP-TDP-43^{A315T} and HiFi-RfxCas13d with a NTG crRNA. **(i-j)** Error bars indicate SEM. *P < 0.05; **P < 0.01; one-tailed unpaired *t*-test.